Pressure Measurement Location Selection in Industrial Gas Headers for Buffering Control

A.J. Wiid[a], J.D. le Roux[a], I.K. Craig[a,*]

[a]*Department of Electrical, Electronic, and Computer Engineering, University of Pretoria, Pretoria, South Africa.*

Abstract

This paper uses a nonlinear model of the pressure and flow dynamics inside a gas header to obtain the optimal pressure measurement location for buffering control. The nonlinear model is derived from governing equations using the spectral element method (SEM). The pressure states at the collocation points are estimated using an extended Kalman filter (EKF) and subsequently used as potential measuring locations. A staggered regulatory pressure control scheme is used to evaluate the closed-loop performance of the objective function in a self-optimising control (SOC) framework. It is found that there are opposing goals in the optimisation scheme and that the final pressure location selection is dependent on the economic importance of these goals. The economic goals which cause opposing control objectives include minimising flaring, providing down-stream consumer stability, and limiting expensive supplier use.

Keywords: gas pipelines, measurement selection, nonlinear modelling, process control applications, self-optimising control, state estimation, spectral element method

1. Introduction

Gas pipe headers in industrial chemical and petrochemical processes are used to transport products in the gas phase from an upstream unit operation to downstream unit operations as a feedstock. Gas header buffering control is challenging as gas exhibits nonlinear behavior with fast integrating dynamics that are sensitive to changes in pressure, composition and temperature.

Large headers behave as integrators, therefore any offset in the mass balance between supplier and consumer results in either flaring or a cut-back. Controlling the mass balance at a dynamic optimum becomes difficult when there are frequent load changes that occur when numerous consumers and suppliers interact on one header. The control of gas headers is typically focused on regulatory control where the pressure is controlled at set-point (SP) and flaring is used to remove gas from the network during high pressure scenarios. This results in valuable product loss, emission penalties and unnecessary energy consumption in upstream processing and gas compression. The problems are particularly evident in large gas to liquid and coal to liquid facilities with gas loops [1]. Due to the fast dynamics of the gas headers, upstream disturbances are quickly propagated through multiple gas circuit units. It is beneficial to reject these disturbances even partially in the gas headers which connect the various process units.

A possible way to address these problems is to use the buffering capacity of the headers to absorb dynamic disturbances. This will minimise flaring and improve the stability of consumer flows. However, buffering capacity is a fixed parameter dependent on the design of the process, and is often dependent on other upstream and downstream process parameters. The influence of process design choices on process control has been an area of interest for many years [2, 3, 4], but a study specifically aimed at gas header design choices could not be found.

As a first step, this study aims to investigate the optimal pressure measurement location under various disturbances and operating conditions. These insights may then be used to assist in the design of controllers for gas headers. The pressure measurement location influences the closed-loop control behaviour due to physical pipe parameters such as friction, diameter, and length.

Self optimising control (SOC) is well suited to find the optimal selection of controlled variables (CVs) given an objective function [5, 6, 7]. SOC techniques are mostly applied to linearised models and are optimised around operating points. As an improvement over the local optimisation techniques, SOC methods were expanded recently so that the CVs are selected based on the global solution space where Monte Carlo simulations are used to evaluate the objective function [8, 9]. SOC is mostly used for static optimisation problems [10] which is not suitable for pressure measurement location selection in gas pipelines because the integrating responses are governed by the mass balance. Therefore, steady-state operation is not of interest but rather the ability to reject cyclic disturbances optimally. Dynamic SOC was recently implemented for batch processes [10], as an extension of the null-space method [11], for an oil reservoir water-flooding process [12], and for robust reservoir management [13].

This study requires a model which can spatially describe the pressure and flow profiles inside a gas header as well as ac-

---

*Corresponding author. Address: Department of Electrical, Electronic, and Computer Engineering, University of Pretoria, Pretoria, South Africa. Tel.: +27 12 420 2172; fax: +27 12 362 5000.

Email address: ian.craig@up.ac.za (I.K. Craig)

curately capture the gas dynamics. To this end, the model developed in [14] and validated on an industrial methane-rich gas network, is chosen. This model uses the spectral element method (SEM) [15, 16] to spatially discretise and solve the partial differential equations as a system of ordinary differential equations (ODEs). The SEM model makes the pipe pressure and flow profiles available at the collocation points.

State estimators are required to evaluate the different pressure measurement locations at the collocation points if online measurements are not available. State estimation has been used for the monitoring [17], simulation [18, 19, 20], leak detection [21, 22, 23, 24, 25], and control [26] of gas pipelines. Kalman filters are well suited for systems that can be described by ODEs [18]. The extended Kalman filter (EKF) was shown to work well for SEM hydraulic applications [27], and was applied successfully to non-linear gas pipeline models [21, 22].

The contribution of this paper is the use of a SEM-based model combined with an EKF to estimate gas header pressure profiles and subsequently evaluate the impact of the pressure measurement location on the pressure control performance using a dynamic SOC framework. More specifically, the pressure measurement location on the pipe length is determined that will provide the buffering control performance required to minimize flaring, expensive supplier intake, and to improve consumer stability.

The paper is organised as follows. Section 2 presents the derivation of the state-space model from the governing equations using the SEM method. Section 3 performs a frequency analysis to illustrate the impact of measurement location on disturbance rejection and controllability, and designs an EKF to provide pressure estimates at unmeasured locations. Section 4 develops a staggered regulatory pressure control scheme for the header model described in Section 2, and evaluates the trade-off between flaring, expensive supplier use, and consumer stability. Section 5 presents the main findings and contribution of this study. The nonlinear SEM model in Section 2, the EKF designed in Section 3, and the PI controllers in Section 4 are used to evaluate the optimal measurement location for different disturbance scenarios. Section 6 concludes the study.

2. Model Development

This section provides a brief summary of the model used for the simulations in this study, and provides a dynamic simulated example of the pressure responses. The model nomenclature is shown in Table 1. (A more detailed model description can be found in [14].)

2.1. Process Description

The process shown in Fig. 1 is an example of a typical process which will be used as the case study for this work. Other configurations are possible. P_z and Q_z are the header inlet pressure and flow rate, and P_L and Q_L are the header outlet pressure and flow rate respectively. The process feed (Q_4) is supplied to the header via a compressor which cannot be manipulated. Gas can be flared at the inlet of the header (Q_1) during high

pressure scenarios and gas can be pulled in from an expensive second supplier (Q_3) during low pressure scenarios. The header outlet supplies gas to one consumer (Q_2). The pipe pressures do not have to be controlled tightly at SP. Q_z and Q_L are calculated using a mass balance as,

$$Q_z = Q_4 + Q_3 - Q_1, \tag{1a}$$
$$Q_L = Q_2. \tag{1b}$$

It is desirable to minimise flaring (Q_1) and expensive supplier use (Q_3), and provide stability for the consumer in the face of load changes from the standard supplier (Q_4).

2.2. Process Model

A general model of gas flow in a pipe is discussed below. This model is used to represent the process in Fig. 1. The pressure and flow dynamics inside a pipe can be described by the continuity (2a) and momentum (2b) equations [28]. The ideal gas law compensated for compressibility (2c) is used to relate the gas properties in the header.

$$\frac{\partial P}{\partial t} + \frac{ZR\,T}{AM_w}\frac{\partial Q}{\partial z} = 0, \tag{2a}$$
$$\frac{\partial Q}{\partial t} + A\frac{\partial P}{\partial z} + \frac{fZR\,TQ|Q|}{2DAM_wP} = 0, \tag{2b}$$
$$PAL - \frac{mZRT}{M_w} = 0. \tag{2c}$$

P is the pressure, Q is the mass flow rate, R is the gas constant, A is the cross sectional area of the pipe, L is the pipe length, Z is the gas compressibility, T is the temperature, f is the coefficient of friction, D the pipe diameter, m is the gas mass, and M_w is the mixed gas molecular weight.

2.3. Weak formulation

Multiplying (2a) and (2b) by a suitable set of test functions v and integrating on the interval $[0, L]$, the weak formulation is written as [16],

$$\int_0^L \frac{\partial}{\partial t}\begin{bmatrix}\kappa P \\ \alpha Q\end{bmatrix}v\,dz = \int_0^L \begin{bmatrix}Q \\ P\end{bmatrix}\frac{\partial v}{\partial z}dz \\ - \int_0^L \begin{bmatrix}0 \\ \tau\,\Theta\end{bmatrix}v\,dz - \begin{bmatrix}Q \\ P\end{bmatrix}\Big|_0^L v, \tag{3}$$
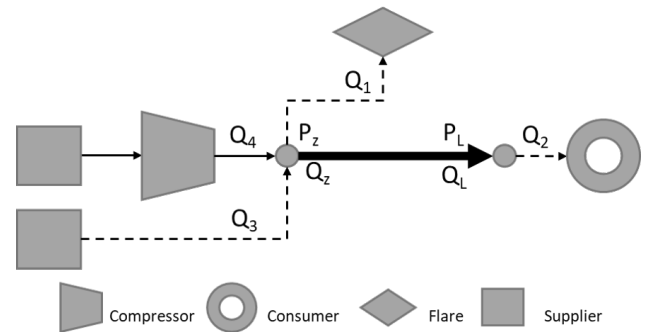

Figure 1: Case study process diagram. The dashed lines indicate streams which may be manipulated and the thick line indicates the header.
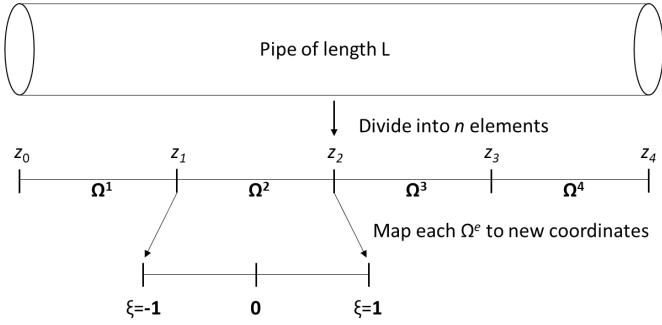
Figure 2: Pipe discretisation into elements and mapping to local coordinates.

where,

$$\kappa = \frac{AM_w}{ZRT}, \quad \alpha = \frac{1}{A}, \quad \tau = \frac{fZRT}{2DA^2M_w}, \quad \Theta = \frac{Q|Q|}{P}. \quad (4)$$

2.4. Pipe Segmentation

The weak formulation in (3) is partitioned into n elements denoted by Ω^e such that $\Omega^e = [z_{e-1}, z_e]$, with $0 = z_0 < z_1 < \cdots < z_e = L$. This results in,

$$\int_{\Omega^e} \frac{\partial}{\partial t} \begin{bmatrix} \kappa P \\ \alpha Q \end{bmatrix} \upsilon dz = \int_{\Omega^e} \begin{bmatrix} Q \\ P \end{bmatrix} \frac{\partial \upsilon}{\partial z} dz - \int_{\Omega^e} \begin{bmatrix} 0 \\ \tau \Theta \end{bmatrix} \upsilon dz, \quad (5)$$

for $e = \{1, \ldots, n\}$. By making use of the mapping function described as,

$$F(\xi)_e = \frac{z_e - z_{e-1}}{2}\xi + \frac{z_e - z_{e-1}}{2}, \quad (6)$$

the element global coordinates, z_e and z_{e-1} for each element, are mapped to a local coordinate system $\xi \in [-1, 1]$. The process of pipe segmentation and mapping is illustrated by Fig. 2. To account for the coordinate transformation inside the integral in (5), the functions have to be multiplied by the Jacobian which, for the one-dimensional case and varying element lengths, can be defined as,

$$J^e = \frac{dz}{d\xi} = \frac{z_e - z_{e-1}}{2}. \quad (7)$$

2.5. Integration

Integration over each element in the interval $\xi \in [-1, 1]$ is performed by making use of the Gauss-Lobatto-Legendre (GLL) quadrature of integration defined as [15],

$$\int_{\Lambda} f^e(\xi)d\xi \approx \sum_{k=0}^{N} \omega_k f^e(\xi_k), \quad (8)$$

where ξ_k and ω_k are the collocation points and integration weights of the GLL quadrature of order N respectively. Calculated values for ξ_k and ω_k are available in literature [15].
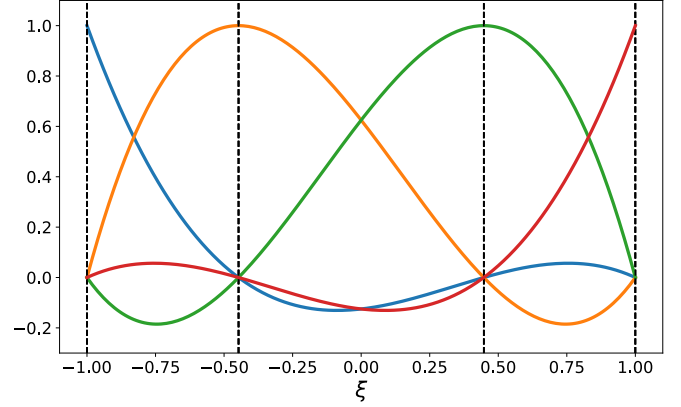

Figure 3: Langrange Polynomials of order 3. The vertical dashed lines indicate the collocation points.

2.6. Interpolation

Barycentric Lagrange interpolation [29] is used to interpolate the element functions. The element functions $f^e(\xi)$ are approximated using the interpolation scheme as,

$$f^e(\xi) \approx \sum_{i=0}^{N} f^e(\xi_i)\ell_i^N(\xi), \quad (9)$$

where f^e is restricted to the segment $[z_{e-1}, z_e]$. Lagrange polynomials ℓ_i^N of order N have the property,

$$\ell_i^N(\xi_j) = \delta_{i,j}, \quad \text{for } j = 0, \ldots, N, \quad (10)$$

where $\delta_{i,j}$ is the Kronecker Delta function. As an example, Lagrange polynomials of order 3 are shown in Fig. 3.

2.7. Mass and Stiffness Matrices

Sections 2.5 and 2.6 are applied to (5) to derive the elemental mass matrices as,

$$(M_\phi)_{ij}^e = \sum_{i=0}^{N} \sum_{k=0}^{N} \phi_i(\xi_k)\omega_k J(\xi_k)\delta_{i,j}, \quad (11)$$

for $j = 0, \ldots, N$ where $\phi \in \{\kappa, \alpha, \tau\}$. The mass matrices are diagonal and non-singular, and can therefore be inverted. Similar to the mass matrices, the elemental stiffness matrices are derived as,

$$S_{ij}^e = \sum_{i=0}^{N} \sum_{k=0}^{N} \omega_k \ell_i'(\xi_k)\delta_{j,k}, \quad (12)$$

for $j = 0, \ldots, N$ where ℓ_i' is the first derivative of the Lagrange polynomial. The global mass (M_ϕ) and stiffness (S) matrices are assembled by diagonally combining the elemental matrices.

2.8. State-space description

The final global system of equations are,

$$\frac{d\boldsymbol{P}}{dt} = M_\kappa^{-1}[S\boldsymbol{Q} + Q_z\boldsymbol{b_0} - Q_L\boldsymbol{b_L}], \quad (13a)$$

$$\frac{d\boldsymbol{Q}}{dt} = M_\alpha^{-1}[S\boldsymbol{P} - M_\tau\boldsymbol{\Theta} + P_z\boldsymbol{b_0} - P_L\boldsymbol{b_L}], \quad (13b)$$

3

and in condensed form,

$$\dot{x} = f(x, u), \qquad (14)$$

where the vectors indicated in bold are defined as,

$$P = [P_1, \ldots, P_c]^T, \qquad (15a)$$

$$Q = [\tilde{Q}_1, \ldots, \tilde{Q}_c]^T, \qquad (15b)$$

$$\Theta = \left[\frac{\tilde{Q}_1 |\tilde{Q}_1|}{P_1}, \ldots, \frac{\tilde{Q}_c |\tilde{Q}_c|}{P_c} \right]^T, \qquad (15c)$$

and c is equal to the total number of collocation points. The flow states in (15b) inherent to the model should not be confused with the process flows in Fig. 1. A tilde ($\sim$) is used to differentiate between the flow states in (15b) and the process flows in Fig. 1. The number of collocation points is dependant on the choice of n and N, and calculated as $nN + 1$. The boundary vectors are of the same length and are defined as,

$$b_0 = [1, 0, \ldots, 0]^T, \qquad (16a)$$

$$b_L = [0, \ldots, 0, 1]^T. \qquad (16b)$$

The boundary conditions Q_z, Q_L, P_z, and P_L for a pipe of length L are defined as,

$$Q_z = Q(0, t) \quad \text{and} \quad Q_L = Q(L, t), \qquad (17a)$$

$$P_z = P(0, t) \quad \text{and} \quad P_L = P(L, t). \qquad (17b)$$

The pipe inlet Q_z and outlet Q_L flows are chosen as model inputs,

$$u = [Q_z, Q_L]^T. \qquad (18)$$

The boundary pressures are given by the following substitutions [16],

$$P_z = P_1 - \sqrt{\frac{ZRT}{M_w}} \frac{AM_w}{2ZRT} (\tilde{Q}_1 - u_1), \qquad (19a)$$

$$P_L = P_c - \sqrt{\frac{ZRT}{M_w}} \frac{AM_w}{2ZRT} (u_2 - \tilde{Q}_c). \qquad (19b)$$

The outputs are the pipe inlet and outlet pressures extracted as the first and last values in the vector P,

$$y = [P_1, P_c]^T = g(x, u). \qquad (20)$$

The outputs are used as measured states for the simulated process in this study.

2.9. State-Space Model Summary

The final state-space model of the system is as follows,

$$\dot{x} = f(x, u), \qquad (21a)$$

$$y = g(x, u), \qquad (21b)$$

where $f(x, u)$ is given by (13), $x = [P^T, Q^T]^T$ as in (15a)-(15b), $u = [Q_z, Q_L]^T$ as in (18), and $y = [P_1, P_c]^T$ as in (20).

2.10. Dynamic Simulation

To showcase the simulation capability of the model and provide a visual representation of the header profile responses, the nonlinear model is initialised at the conditions shown in Table 1, and provided with a sequence of inputs to Q_z and Q_L. P_L is initialised from P_z using a simplification of (2b) [30]. The states are initialised by interpolating between the boundary conditions. For $n = 2$ and $N = 3$, there are 7 collocation points along the length of the pipe. P_1 to P_7 in (15a) represent the pressures at the 7 collocation points with $c = 7$. P_1 and P_7 are the pressure states at the inlet and outlet of the pipe respectively. The simulation is propagated using the fourth order Runge-Kutta explicit time discretization scheme.

Table 1: Model initialisation values.

Parameter	Value	Units
Initial Inlet Pressure (P_z)	3000	kPa
Initial Outlet Pressure (P_L)	$P_z - \frac{fZRTQ|Q|L}{2DA^2M_wP_z}$	kPa
Initial Mass Flow (Q)	10	kg/s
Friction (f)	0.2	-
Compressibility (Z)	0.95	-
Gas Constant (R)	8314.47	J/kmolK
Temperature (T)	300	K
Molecular Weight (M_w)	17.2	kg/kmol
Pipe length (L)	5000	m
Pipe Diameter (D)	0.5	m
Pipe Segments (n)	2	-
Polynomial Order (N)	3	-
Time step size (Δt)	1	s

The pressure responses are shown in Fig. 4. Mass balance off-set, when Q_z and Q_L are not the same, has an integrating pressure response, and flow rate changes have first-order self-regulating pressure responses. It is important to note that the integrating gain is the same at all the collocation points but the self-regulating responses vary in magnitude and direction depending on the collocation point.

Fig. 5 shows where the pressure measurements are located on the header at the collocation points for a choice of $n = 2$ and $N = 3$ as well as the upstream and downstream directions as used in this study.

3. Model Analysis and State-Estimation

The pressures at the collocation points on the plant are not measured. Therefore, a state-estimator is necessary to estimate the pressures so that they can be used for feedback control. Section 3.1 completes a controllability and observability analyses of the model in Section 2, Section 3.2 performs a frequency analysis, and Section 3.3 develops a suitable observer to estimate the unmeasured pressures followed by a simulation to test
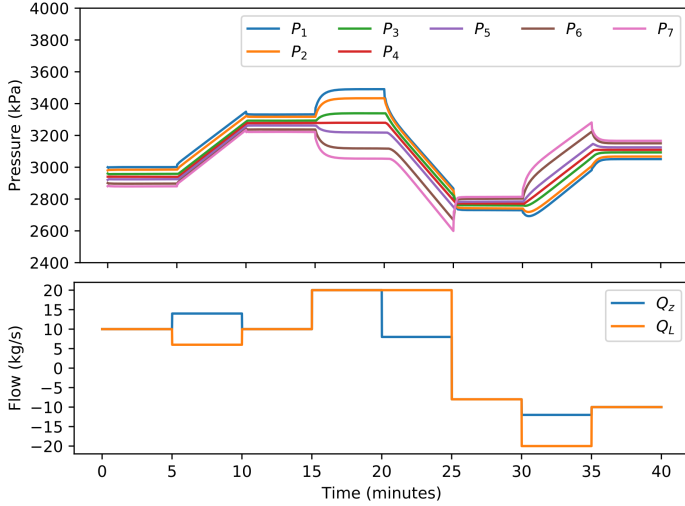
4

Figure 4: Dynamic responses of the states $\boldsymbol{P}$ in (15a) given flow inputs to Q_z and Q_L.
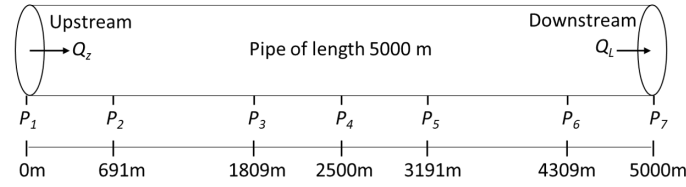

Figure 5: Locations of the pressures measurements P_1 to P_7 on the header.

the EKF accuracy in Section 3.4. As shown in Section 5, the EKF provides feedback to the PI controllers designed in Section 4 to evaluate the optimal measurement locations.

3.1. State Controllability and Observability

It is desirable to use a minimal realisation of a system for simulation and analysis. To this end a state controllability and observability analysis is done. Additionally, state observability is essential for the design of state estimators. The linearised state-space description has the form,

$$\delta \dot{\boldsymbol{x}} = A\delta \boldsymbol{x} + B\delta \boldsymbol{u}, \tag{22a}$$

$$\delta \boldsymbol{y} = C\delta \boldsymbol{x} + D\delta \boldsymbol{u}. \tag{22b}$$

This formulation is obtained from the nonlinear equations of Section 2 by obtaining the first order Taylor series expansion of the functions $\boldsymbol{f}(\boldsymbol{x}, \boldsymbol{u})$ and $\boldsymbol{g}(\boldsymbol{x}, \boldsymbol{u})$ in (21) with respect to $\boldsymbol{x}$ and $\boldsymbol{u}$ at a chosen steady state operation $\boldsymbol{x} = \boldsymbol{x}_0$ and $\boldsymbol{u} = \boldsymbol{x}_0$. The deviation variables are defined as $\delta \boldsymbol{x} = \boldsymbol{x} - \boldsymbol{x}_0$, $\delta \boldsymbol{u} = \boldsymbol{u} - \boldsymbol{u}_0$, and $\delta \boldsymbol{y} = \boldsymbol{y} - \boldsymbol{y}_0$. The matrices A, B, C and D for the equilibrium condition in Table 1 are shown in Appendix A.

The number of states is calculated as $2(nN + 1)$. The linear state-space model (22) is found to be state controllable and observable for choices of $N = 3$ and $n = 2$. Therefore, (22) represents a minimal realisation [7]. The nonlinear state-space model will be observable if the linearised state-space model is observable [31, 32].

3.2. Measurement Location Frequency Analysis

In this section two concepts are illustrated in the frequency domain:

Table 2: Input and output scaling factors.

Parameter	Scaling Value	Unit
Pressure	5000	Pa
Flows	5	kg/s

1. The pipe distance between the chosen measurement location and the final control element influences the ability to control the plant.
2. The pipe functions as a filter which is beneficial for disturbance rejection.

The Laplace transform of (22) results in the following transfer function,

$$\hat{G}(s) = \begin{bmatrix} \delta P_1(s)/\delta Q_z(s) & \delta P_1(s)/\delta Q_L(s) \\ \delta P_c(s)/\delta Q_z(s) & \delta P_c(s)/\delta Q_L(s) \end{bmatrix}, \tag{23}$$

where $\hat{G}(s)$ is calculated from (22) as,

$$\hat{G}(s) = C(sI - A)^{-1}B + D. \tag{24}$$

For Section 3.2, the plant model ($\hat{G}_p(s)$) and the disturbance model ($\hat{G}_d(s)$) are defined as,

$$\hat{G}_p(s) = \hat{G}_{22}(s), \tag{25a}$$

$$\hat{G}_d(s) = \hat{G}_{21}(s). \tag{25b}$$

Therefore, $\hat{G}_p(s)$ and $\hat{G}_d(s)$ are the unscaled transfer functions between the outlet flow rate (Q_L) and the inlet flow rate (Q_z) to the chosen downstream pressure measurement (P_c) respectively. The measurement location is chosen by varying the pressure output in the second row of the C matrix in (22) as one of the $c = 7$ collocation points.

The process is scaled as proposed by [7] and the scaling factors used to obtain the scaled transfer functions G_p and G_d are shown in Table 2. The scaled linear model for $\delta P_c(s)$ is written as,

$$\delta P_c(s) = G_p(s)\delta Q_L + G_d(s)\delta Q_z. \tag{26}$$

The remaining process parameters are unchanged as specified in Table 1. The values for $|G_p(j\omega)|$ and $|G_d(j\omega)|$ over a frequency range when varying the measurement locations from P_1 to P_7 are shown in Fig. 6a and Fig. 6b respectively.

The values for $|G_d(j\omega)|$ are almost identical to $|G_p(j\omega)|$ but reversed in relation to the measuring location choice (i.e the values of $|G_p(j\omega)|$ at P_7 in Fig. 6a are similar to the values for $|G_d(j\omega)|$ in Fig. 6b at P_1). Therefore, choosing a measurement location which is closer to the disturbance source (Q_z) than the final controlled element (Q_L) may result in $|G_p(j\omega)| < |G_d(j\omega)| - 1$, depending on the scaling, which is undesirable for control [7]. At P_4, $|G_p(j\omega)| \approx |G_d(j\omega)|$ because P_4 is equidistant from the disturbance source at Q_z and the final control element at Q_L. The impact of measurement location choice is reduced at lower frequencies.

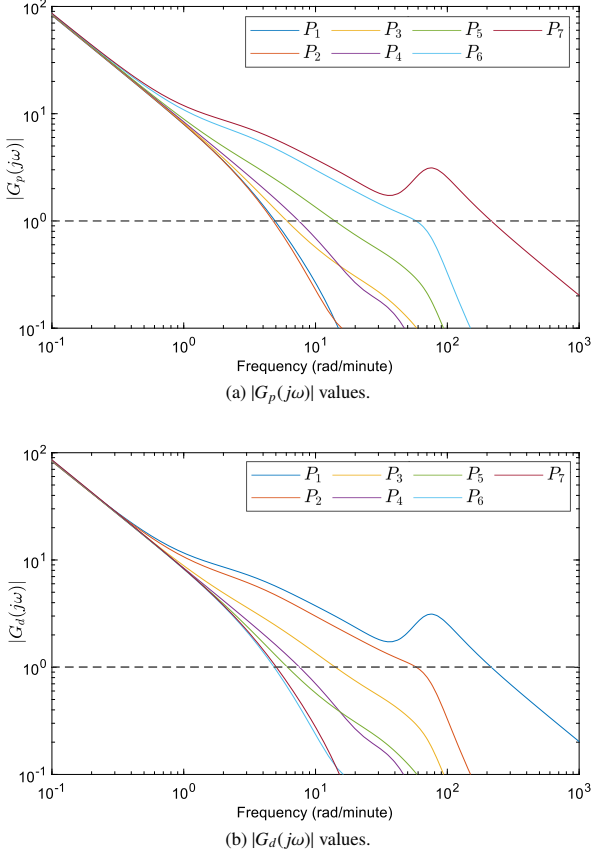Therefore, Fig. 6 illustrates the following two concepts:

5

(a) $|G_p(j\omega)|$ values.

(b) $|G_d(j\omega)|$ values.

Figure 6: $|G_p(j\omega)|$ and $|G_d(j\omega)|$ values for measurement location choices at P_1 to P_7.

- The further the pressure measurement is from the manipulated variable, Q_L, the more difficult it is to control the plant due to the dynamic effect taking longer to reach the measurement as indicated by the locations where $|G_p(j\omega)|$ crosses the line $|G_p(j\omega)| = 1$.

- The pipe between the measurement and the flow disturbance filters out high frequency signals [33], as indicated by the locations where $|G_d(j\omega)|$ crosses the line $|G_d(j\omega)| = 1$, which is advantageous for disturbance rejection.

The ability to reject disturbances and control the plant based on measurement location is further investigated in Section 5.

3.3. Extended Kalman Filter

Since the plant model described in (14) and (20) is state observable as discussed in Section 3.1, an EKF will be used to provide suitable state estimators for the internal pressures at the collocation points. The model in (21) is rewritten in discrete form as,

$$x_{k+1} = f_k(x_k, u_k) + d_k, \quad (27a)$$
$$y_k = Cx_k + v_k, \quad (27b)$$

where $x = [P^T, Q^T]^T$, d_k is the process noise with covariance $\hat{Z} > 0$, and v_k is the measurement noise with covariance $\hat{R} > 0$.

The matrix C extracts the desired pressure values from x_k. The discrete process model is expressed as an implicit trapezoidal integration scheme,

$$x_{k+1} = x_k + \frac{\Delta t}{2}\big(f_k(x_{k+1}, u_k) + d_{k+1} + f_k(x_k, u_k) + d_k\big), \quad (28)$$

and solved using the Newton-Raphson method. As shown in (28), zero-order hold is applied to the input vector. The *a-priori* estimate $(\hat{x}_k^-)$ and estimation error covariance matrix $(\hat{H}_k^-)$ is solved as [32],

$$\hat{x}_{k+1}^- = f_k(\hat{x}_k^+, u_k), \quad (29)$$
$$\hat{H}_{k+1}^- = W_k\hat{H}_k^+ W_k^T + V_k\hat{Z}_k V_k^T, \quad (30)$$

where $\hat{x}_k^+$ is the posterior state estimate. W_k and V_k are the partial derivatives of f_k to the states x_k and process noise d_k respectively, and have the discrete forms,

$$W_k = \frac{\partial f_k}{\partial x_k},$$
$$= -\left(I - \frac{\Delta t}{2}\left(\frac{\partial f_k}{\partial x_{k+1}}\bigg|_{\hat{x}_k, u_k}\right)\right)^{-1}\left(-I - \frac{\Delta t}{2}\left(\frac{\partial f_k}{\partial x_k^+}\bigg|_{\hat{x}_k, u_k}\right)\right), \quad (31)$$

and,

$$V_k = \frac{\partial f_k}{\partial d_k} = \frac{\Delta t}{2}\left(I - \frac{\Delta t}{2}\left(\frac{\partial f_k}{\partial x_{k+1}}\bigg|_{\hat{x}_k, u_k}\right)\right)^{-1}. \quad (32)$$

The observer measurement correction is [32],

$$k_k = \hat{H}_k^- C^T\big(C\hat{H}_k^- C^T + \hat{R}_k\big)^{-1}, \quad (33)$$
$$\hat{H}_k^+ = \big(I - \hat{k}_k C\big)\hat{H}_k^-, \quad (34)$$
$$\hat{x}_k^+ = \hat{x}_k^- + k_k\big(y_k - C\hat{x}_k^-\big), \quad (35)$$

where k_k is the Kalman gain. The state estimations and covariance matrices are initialised as,

$$\hat{x}_0^+ = x_0, \quad (36a)$$
$$\hat{Z}_k = \mathrm{diag}(\hat{Z}_P I, \hat{Z}_Q I), \quad (36b)$$
$$\hat{R}_k = \mathrm{diag}(\hat{R}_P I, \hat{R}_Q I). \quad (36c)$$

$\hat{Z}_P$, $\hat{Z}_Q$, $\hat{H}_0^- > 0$ are tuning parameters. $\hat{R}_P$ and $\hat{R}_Q$ are chosen using typical instrument accuracies.

3.4. State Estimation Accuracy

The simulation environment to test the EKF is created as follows:

- A sinusoidal disturbance is injected into the system with an amplitude of 5 kg/s and a period of 1 minute: $Q_z = 5\sin(2\pi/60 t)$.

- The pressure states are sub-optimally initialised at the average header pressure to observe how they converge to the true state values: $P_{c,k=0} = (P_z + P_L)/2$ for $c \in [1, \ldots, 7]$.
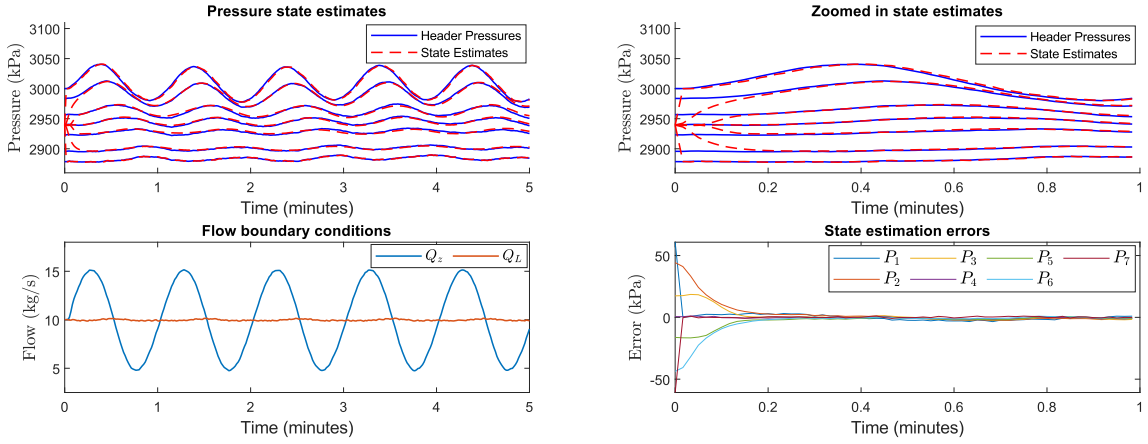
6

Figure 7: Model simulated states compared to state estimations for pressures at the collocation points P_1 to P_7, the state estimation errors, and the flows Q_z and Q_L at the boundary conditions.

- Measurement noise is added to the outputs: $v_k \sim \mathcal{N}(0, \sigma_v^2)$.

- Process noise is added to the plant pressure and flow states respectively: $d_{k_P} \sim \mathcal{N}(0, \sigma_{d_P}^2)$, $d_{k_Q} \sim \mathcal{N}(0, \sigma_{d_Q}^2)$.

- $\hat{H}_0^-$ is initialized as a matrix of ones.

- The simulation is propagated over time using an explicit fourth order Runge-Kutta algorithm for a time frame of 5 minutes and a sampling period of $\Delta t = 1$ s.

The state estimation parameters used in the simulation environment are shown in Table 3 and the remaining parameters are initialised as shown in Table 1.

Table 3: EKF parameters.

Parameter	Value	Unit
$\hat{Z}_P$	1	kPa
$\hat{Z}_Q$	0.1	kg/s
$\hat{R}_P$	3	kPa
$\hat{R}_Q$	0.2	kg/s
σ_v^2	1	kPa
$\sigma_{d_P}^2$	3	kPa
$\sigma_{d_Q}^2$	0.1	kg/s

The results are shown in Fig. 7 and it can be seen that the state estimates converge to the true states. The root mean squared error (RMSE) of all the pressures for the time period after the states have converged ($t > 0.3$ minutes) is shown in Table 4. From Table 4 it can be seen that the states are accurately estimated by the EKF given the process and measurement noise in Table 3.

The damping effect of the pipe length discussed in Section 3.2 can be seen in Fig. 7 where the sine waves have phase lag and a decreased amplitude as the pipe length increases [34]. The combination of using the SEM model to provide pressure

Table 4: State estimation errors.

Measurement Location	RMSE (kPa)
P_1	4.9
P_2	2.8
P_3	7.1
P_4	3.9
P_5	7.1
P_6	2.1
P_7	0.6

profiles and using an EKF to attain the estimated states is attractive for applications that require pressures values at non-measured locations. The flow states Q in (15b) can be estimated in a similar manner.

4. PI Control for Pressure Buffering

This section develops a typical control scheme to use for the case study process in Fig. 1 using PI controllers. The header control scheme and controller tuning rules are described in Section 4.1. Section 4.2 describes how the controller error E_k is calculated and how the SPs and process values (PVs) are determined, and Section 4.3 provides a closed loop simulation introducing the trade-off between flaring, expensive supplier use, and consumer stability. The PI controllers developed here are used in Section 5 to determine the optimal measurement locations.

4.1. PI Tuning

PID controllers may vary in their exact implementation depending on the application. The typical solution to pressure control is the standard PI controller represented in discrete velocity form as,

$$\mathcal{M}_{k+1} = \mathcal{M}_k + K_c\Big[(E_k - E_{k-1}) + \frac{\Delta t}{\tau_I}E_k\Big], \qquad (37)$$

7

where E_k is the error, K_c is the controller gain, τ_I is the integral time, and $\mathcal{M}_k$ is the controller output at time step k.

The process gain (K) used for the tuning rules is derived from (2c) as [30],

$$\frac{dP}{dt} = \frac{ZRT}{ALM_w}\left(Q_z - Q_L\right), \tag{38}$$

where the integrating gain of the pressure response is approximated as,

$$K \approx \frac{ZRT}{ALM_w}. \tag{39}$$

The simple internal model control (SIMC) tuning rules proposed for integrating processes by [35] are as follows,

$$K_{c,1} = \frac{1}{K(\tau_c + \theta)}, \tag{40a}$$

$$\tau_I = 4(\tau_c + \theta). \tag{40b}$$

Following the reasoning in [36], the buffering controller gain ($K_{c,1}$) is chosen and used to solve for the desired closed loop time constant (τ_c) and process delay (θ), which is then used to solve for the controller time constant (τ_I).

The gain of the buffering pressure controller is chosen as,

$$K_{c,1} = \frac{Q_{max}}{P_{max}}, \tag{41}$$

from which $\tau_c + \theta$ and τ_I is solved using (40). Q_{max} is the maximum allowed consumer flow rate (Q_2) deviation from the initialised value and P_{max} is the maximum allowed pressure deviation from SP at the chosen measurement location. Q_{max} is chosen as 5 kg/s and P_{max} is chosen as 100 kPa in this study.

A staggered pressure control scheme is used to control the header pressure in Fig. 1. A buffering pressure PI controller is used to control Q_2, an under pressure PI controller is used to control Q_3 during low pressure scenarios, and an over pressure PI controller is used to control Q_1 during high pressure scenarios. In this work the controller gains for the under and over pressure controllers ($K_{c,2}$) are adapted from the tight level control heuristics given in [37] for header pressure control as,

$$K_{c,2} = \frac{0.4}{KQ_{max}}, \tag{42}$$

and the integral time used for the buffering controller is also used for the over and under pressure controllers.

The over pressure controller (43a), buffering pressure controller (43b), and under pressure controller (43c) are described as,

$$Q_{1,k+1} = Q_{1,k} + K_{c,2}\left[(E_{1,k} - E_{1,k-1}) + \frac{\Delta t}{\tau_I}E_{1,k}\right], \tag{43a}$$

$$Q_{2,k+1} = Q_{2,k} + K_{c,1}\left[(E_{2,k} - E_{2,k-1}) + \frac{\Delta t}{\tau_I}E_{2,k}\right], \tag{43b}$$

$$Q_{3,k+1} = Q_{3,k} - K_{c,2}\left[(E_{3,k} - E_{3,k-1}) + \frac{\Delta t}{\tau_I}E_{3,k}\right]. \tag{43c}$$

The PI controller tuning parameters are given in Table 5. The tuning rules developed are independent of the pressure measuring location because the integrating gains are the same for all the pressure measurement locations as shown in Fig. 4.

Table 5: Tuning values.

Parameter	Value	Units
K	140.32	Pa/kg
τ_I	570	s
$K_{c,1}$	0.05×10^{-3}	kg/Pa.s
$K_{c,2}$	0.57×10^{-3}	kg/Pa.s
$\tau_c + \theta$	143	s

4.2. PI Controller References and Feedback

The measurement locations for the buffering pressure controller (p), and the over and under pressure controllers (o) are selected as one of the $c = 7$ collocation points and provided to the PI controllers as PVs.

The SP of the buffering controller is given a value equal to the initialised pressure value for the selected collocation point at p. The over and under pressure controllers receive a SP equal to P_{max} above and below the initialised value of the buffering controller respectively. The value of P_{max} is an engineering decision based on the process design and alarm limits. Therefore, because o and p can potentially be measured at the inlet and outlet of the header respectively, P_{max} should be chosen carefully to ensure that the pressure controller SPs do not become coupled through the header pressure drop. The controller SPs are given as,

$$\bar{r} = P_{p,k=0} + P_{max}, \tag{44a}$$

$$r = P_{p,k=0}, \tag{44b}$$

$$\underline{r} = P_{p,k=0} - P_{max}, \tag{44c}$$

where $\bar{r}$, $\underline{r}$ and r are the SPs for the over (43a), under (43c) and buffering (43b) pressure controllers respectively. It is important to note that $\bar{r}$ and $\underline{r}$ are defined relative to the buffering controller measuring location p in this study because the header will operate at r when no disturbances are present. The controller errors in (43) are defined as,

$$E_{1,k} = \bar{r} - P_{o,k}, \tag{45a}$$

$$E_{2,k} = r - P_{p,k}, \tag{45b}$$

$$E_{3,k} = \underline{r} - P_{o,k}. \tag{45c}$$

4.3. Closed Loop Simulation

A simulation of the control scheme is shown in this section highlighting the response of the buffering controller using the tuning rules presented in Section 4.1 and the impact of the over and under pressure controllers on the overall performance.

A sinusoidal disturbance is injected into the system through Q_4 with an amplitude of 5 kg/s and a period of 20 minutes. o and p are selected as 4. Therefore, the over and under pressure controllers, and the buffering pressure controller use P_4 as a measurement location in this simulation. The remaining parameters are initialised as shown in Table 1. The simulation time is 70 minutes and the results are shown in Fig. 8.
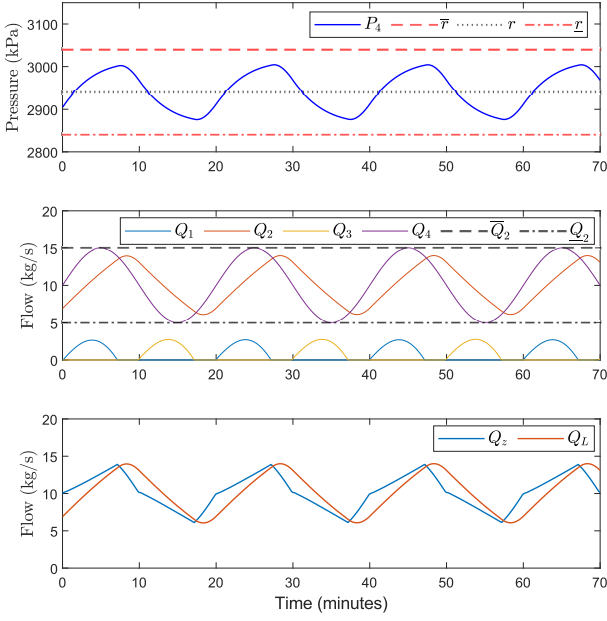
Figure 8: Closed loop simulation.

It can be seen from Fig. 8 that the output of the buffering pressure controller (Q_2) moves slowly between the consumer low limit ($\underline{Q}_2$) and high limit ($\bar{Q}_2$) which is determined by Q_{max}. As P_4 approaches the high and low limits the under pressure and over pressure controllers take action as shown by the movement in Q_1 and Q_3. It is desirable to tune the PI controllers so that P_4 does not come too close to the pressure limits $\bar{r}$ and $\underline{r}$. Otherwise, slightly larger than expected disturbances and process noise may cause nuisance alarms and in extreme cases process upsets such as the lifting of pressure safety valves. The SEM model inputs (Q_z and Q_L) are also shown in Fig. 8 and are calculated using (1).

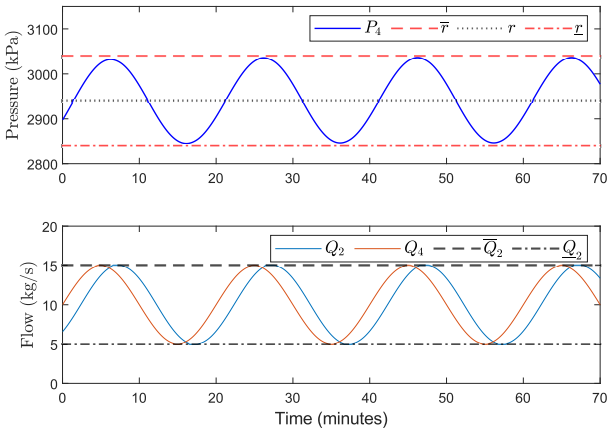Fig. 9 shows the simulation results when the over and under pressure controllers are disabled. It can be seen in Fig. 9 that P_4 moves a lot closer to the pressure limits $\bar{r}$ and $\underline{r}$ and that the output of the buffering pressure controller saturates at the output limits $\underline{Q}_2$ and $\bar{Q}_2$. Q_2 and Q_4 is equal to Q_z and Q_L respectively in Fig. 9 (refer to (1)).

The sum of incremental changes for Q_2 is described as,

$$\sum_{k=1}^{S} \left| \frac{Q_{2,k} - Q_{2,k-1}}{\Delta t} \right|, \tag{46}$$

where S is the total amount of time steps and k is the current time step. The absolute change in Q_2 is defined as the difference between the maximum value and the minimum value observed from Q_2 in the simulations. Table 6 shows the sum of incremental changes and the absolute change observed in Fig. 8 and Fig. 9.

Table 6: Performance metrics for Fig. 8 and Fig. 9.

Consumer Flow (Q_2) Stability Metric	Fig. 8	Fig. 9
Sum of Incremental Changes (kg)	277.4	350.3
Absolute Change (kg/s)	7.94	10

It can be seen from Table 6 that the over and under pressure controllers assist in providing improved consumer stability as the sum of the incremental changes and absolute change is lower in Fig. 8 than Fig. 9. However, this has an added cost of flaring and expensive supplier use which is investigated further in Section 5.

5. Optimal Pressure Measurement Location

This section contains the main contribution of this study. It describes the simulation approach to find the optimal pressure measurement locations and shows how the cost functions are evaluated. As shown in the simulation setup in Fig. 10, the nonlinear SEM model in Section 2, the EKF designed in Section 3, and the PI controllers in Section 4 are used in conjunction to evaluate the optimal pressure measurement locations.

5.1. Pressure Constraints

The over and under pressure controllers, which influence the header inlet flow rate, should not receive a pressure measure-
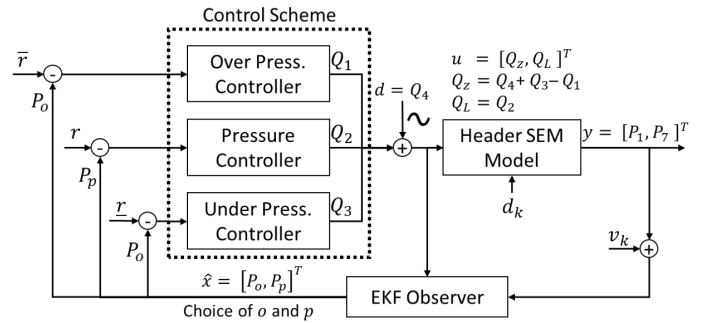

Figure 9: Closed loop simulation with over and under pressure controllers disabled.

Figure 10: Block diagram of the simulation framework.

9

ment which is further downstream than the pressure measurement received by the buffering controller which controls the outlet header flow rate. This restriction is due to the phase lag between the measurement and the final control element which may result in instabilities as discussed in Section 3.2. This restriction, mathematically given as $p \geq o$, eliminates a large portion of the potential p and o pairings.

It is assumed in this study that the header operates far enough from design and alarm limits so that the pressures at upstream and downstream collocation points do not violate pressure limits if the pressure is controlled at any choice of p and o. In the event that such violations do occur the pressure violation would have to be quantified and included as constraints. If $p \geq o$ holds, the upstream pressure constraint (47a) and downstream pressure constraint (47b) can be mathematically expressed as,

$$\underline{P}_o < P_p + \frac{fZRTQ|Q|(L_p - L_o)}{2DA^2 M_w P_r} < \bar{P}_o, \qquad (47a)$$

$$\underline{P}_p < P_o - \frac{fZRTQ|Q|(L_p - L_o)}{2DA^2 M_w P_r} < \bar{P}_p, \qquad (47b)$$

where L_p is the length of P_p from the header inlet and L_o is the length of P_o from the header inlet. $\bar{P}_o$ and $\underline{P}_o$ are the high and low pressure limits of P_o respectively, $\bar{P}_p$ and $\underline{P}_p$ are the high and low pressure limits of P_p respectively, and P_r is a pressure reference which was chosen as P_z in Table 1. Notice that if the pressures and corresponding limits are selected at the same locations, $L_o = L_p$, the pressure drop term becomes zero and the constraint becomes $\underline{P}_{o=p} < P_{o=p} < \bar{P}_{o=p}$. A typical solution is to measure for over pressure protection at the header inlet and under pressure protection at the header outlet thereby ensuring that alarm and design limits are met across the header.

5.2. Cost Evaluation

The problem is how to choose the optimal pressure measurement locations so that the control system can optimally use the header buffering capacity to meet the process goals: minimise flaring and expensive supplier use, and provide consumer stability.

The cost of flaring (J_1), consumer stability (J_2) and expensive supplier use (J_3) is expressed as,

$$J_1 = \frac{\sum_{k=1}^{S} Q_{1,k}}{S\,W_1}, \qquad (48a)$$

$$J_2 = \frac{1}{S\,W_2} \sum_{k=1}^{S} \left| \frac{Q_{2,k} - Q_{2,k-1}}{\Delta t} \right|, \qquad (48b)$$

$$J_3 = \frac{\sum_{k=1}^{S} Q_{3,k}}{S\,W_3}. \qquad (48c)$$

Therefore, (J_1) is associated with the over pressure controller (43a), (J_2) is associated with the buffering pressure controller (43b), and (J_3) is associated with the under pressure controller (43c). The total loss function (J_T) is,

$$J_T = J_1 + J_2 + J_3. \qquad (49)$$

S is the total amount of time steps, k is the current time step, and the weights W_1, W_2, and W_3 are used to scale the individual loss functions relative their economic penalty. The weights are chosen as shown in Table 7.

Table 7: Cost function weights.

Weight	Value
W_1	3.5
W_2	0.018
W_3	1.1

Similar to [12] and [13] a scenario based approach is used to select the optimal measurement location. The optimal pressure measurement locations are determined for varying sine wave disturbance amplitudes and frequencies. Disturbances are explicitly induced and the objective function evaluated in a simulation environment using a brute-force SOC method [6, 7] and evaluated for every pairing of p and o where $p \geq o$. This methodology was chosen to overcome the following obstacles:

- The over and under pressure controllers introduce nonlinearities at the saturation boundaries.

- The cost functions need to be evaluated dynamically.

- Typical industrial header disturbances are oscillatory in nature due to upstream and downstream process changes such as equipment sequences, hourly demand cycles, and controller tuning.

- The interaction between the over and under pressure controllers and the buffering pressure controller is dependent on the selected measuring locations.

- Information regarding the gradual change in the cost incurred when varying the measurement location is as valuable as finding the optimal measuring locations.

- To demonstrate the effectiveness of the methodology, all the costs for the scenarios are shown as opposed to only providing the optimal measurements.

- The measurement location changes the apparent operating region of the header as the further downstream the pressure is measured, the lower the header pressure is perceived to be. Controlling the header pressure at chosen locations changes the variability of the upstream and downstream location pressures. This is important to consider when the header pressure controller and the over and under pressure controllers do not use the same measuring locations.

5.3. Results and Discussion
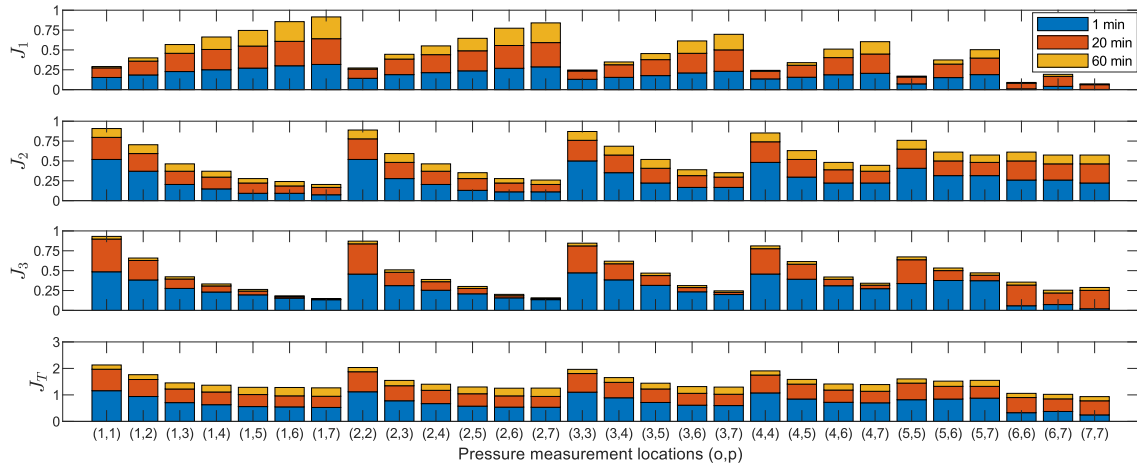
The disturbance sine wave amplitude is given three values: $0.75Q_{max}$, Q_{max}, and $1.25Q_{max}$ with an initial value equal to the consumer flow Q_2. The sine wave frequency is changed by choosing the sine wave period to be: 1 minute, 20 minutes, and 60 minutes. This results in a total of 9 scenarios which capture small, typical, and large disturbance as well as fast, medium and
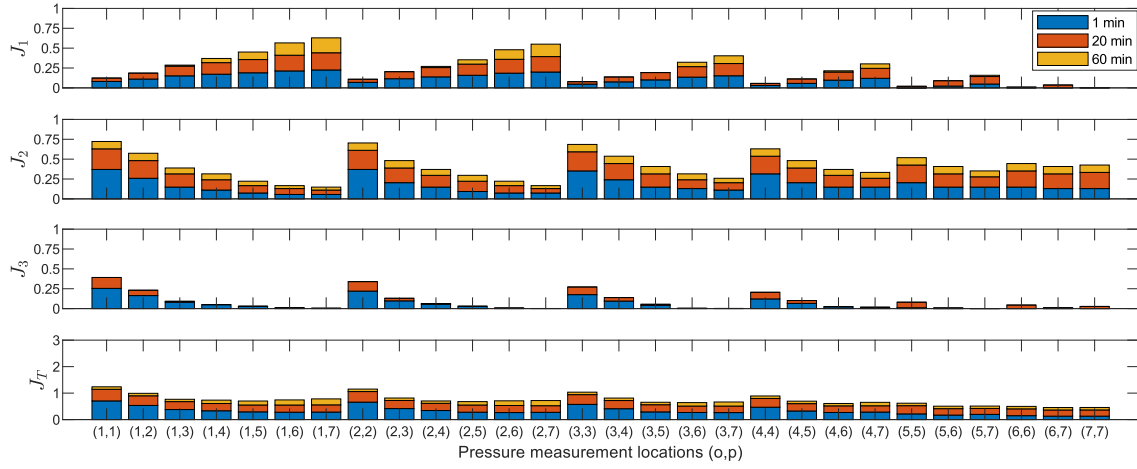
(a) Loss functions for a sine wave disturbance amplitude of $0.75Q_{max}$.
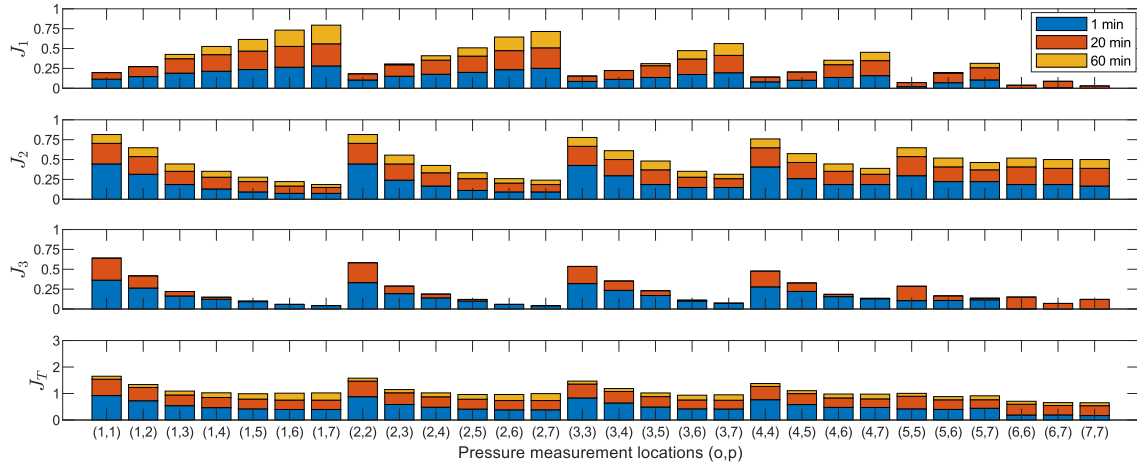
(b) Loss functions for a sine wave disturbance amplitude of Q_{max}.

(c) Loss functions for a sine wave disturbance amplitude of $1.25Q_{max}$.

Figure 11: Associated costs for choices of p and o given disturbance sine wave amplitudes of $0.75Q_{max}$, Q_{max}, and $1.25Q_{max}$ at periods of 1, 20, and 60 minutes. J_1 is the cost of flaring associated with the over pressure controller, J_2 is the cost of consumer stability associated with the buffering controller, and J_3 is the cost of expensive supplier use associated with the under pressure controller. J_T is the sum of all costs.

slow disturbances. The remaining parameters are initialised as shown in Table 1, Table 3, and Table 5. The results are shown in Fig. 11 and the following observations are made:

- As the measurement location for the buffering pressure controller (p) moves downstream on the header, the cost of flaring (J_1) increases while the cost of using the expensive supplier (J_3) decreases. The difference in direction between the over and under pressure cost functions is due to the real available buffering capacity changing size as p moves downstream on the header. This is due to the header pressure drop influencing the available buffering capacity between o and p as shown by (47). The opposing directions of the over and under pressure control costs have a balancing effect on the total cost which is influenced by the economic weights W_1 and W_3.

- As the measurement location for the buffering pressure controller (p) moves downstream on the header, the cost of consumer stability (J_2) decreases. This is in agreement with the findings of Section 3.2 because the header pressure becomes more controllable when the distance between the measurement and the final control element decreases which allows the controller to take less action when controlling the pressure.

- At lower frequencies and lower disturbance magnitudes the buffering controller is able to effectively mitigate flaring and expensive supplier usage as expected. This is seen where there is no flaring or expensive supplier use for a disturbance period of 60 minutes for some choices of p and o.

- A choice of $o \geq 6$ and $p \geq 6$ for sine wave disturbance amplitudes of $0.75Q_{max}$ and Q_{max} is particularly interesting. Flaring and expensive supplier use for a disturbance with the largest sinewave period of 60 minutes are mitigated by the averaging controller. The disturbance with the smaller sinewave period of 1 minute is absorbed by the pipe which functions as a filter as shown in Fig. 6.

- In general, the locations where $p = o$ have higher associated costs for expensive supplier use (J_3) and consumer stability (J_2), but lower associated costs for flaring (J_1). This is noteworthy as this is a standard measuring configuration on industrial headers.

- A selection of p and o which is close to the header outlet has the lowest associated total costs given the chosen economic weights W_1, W_2, and W_3. This is attributed to the filtering effect of the header length between the disturbance and the measurement location, and the short distance between the measurement location and the buffering pressure controller output Q_2.

- At low frequencies the under pressure controller has to take less action than the over pressure controller. This is seen by the reduction in the cost contribution of the under pressure controller (J_3) for disturbances with a period of 60 minutes.

- For the current process layout and control structure it can be seen that if the cost function weights are such that the costs are similar, the total costs become similar for all the different disturbance signals applied. Therefore, depending on the economic costs the difference in measurement location may become negligible.

From these observations it is clear that the optimal measurement location is dependant on the economic objectives of the header, the size and frequency of the sinusoidal disturbances, and if the control action influences the inlet or outlet header flow rate.

Fig. 11a and Fig. 11b indicate that for the disturbances of amplitude $0.75Q_{max}$ and Q_{max}, the pressure measurement location should be selected close to the header outlet. However, there are exceptions as highlighted by the optimal measurement locations for the disturbances of amplitude $1.25Q_{max}$ shown in Table 8. The disturbances of amplitude $1.25Q_{max}$ is used because there are unique optimum values for each scenario. This is due to the large disturbance amplitude which makes it impossible for the buffering controller to reject, or the pipe to absorb, the disturbances.

Table 8: Optimal reference locations for disturbance sizes of $1.25Q_{max}$.

Amplitude	Period	Reference Location (o, p)		
(kg/s)	(min)	$J_1 + J_3$	J_2	J_T
$1.25Q_{max}$	1	7,7	1,7	7,7
$1.25Q_{max}$	20	7,7	1,7	2,7
$1.25Q_{max}$	60	7,7	2,7	4,4

It can be seen from Table 8 that the optimal pairing is dependent on the period of the disturbance. If flaring and expensive supplier use is important then the optimal pairing is ($o = 7, p = 7$) for all the periods used. If consumer stability is important then a pairing of ($o = 1, p = 7$) provides the best cost at lower periods whereas ($o = 2, p = 7$) provides the best cost at the largest period. It can be seen that the combined total cost varies for each disturbance period with a pairing of ($o = 7, p = 7$), ($o = 2, p = 7$), and ($o = 4, p = 4$) providing the best total cost for periods of 1 minute, 20 minutes and 60 minutes respectively.

At typical (Q_{max}) and small ($0.75Q_{max}$) disturbance magnitudes there are multiple pairings which are optimal due to the buffering pressure controller or the pipe being able to completely absorb the disturbances. An example is shown in Fig. 12 where sinusoidal disturbances with periods of 1 minute, 20 minutes and 60 minutes are injected into the system with an amplitude of Q_{max}. o and p are chosen as 7.

Fig. 12a shows that at a small period of 1 minute the pipe filters out the fast disturbance signals such that the pressure at P_7 does not deviate substantially from the SP. Therefore, the over and under PI controllers do not react and there is no deviation in Q_1 and Q_3.

Fig. 12b shows that at a medium period of 20 minutes the over and under pressure controllers assist to control the pres-

sure. The over and under pressure controllers need to assist in Fig. 12b because the disturbance signal is too fast to be rejected completely by the slower tuned buffering controller but is slow enough that the pipe which acts as a filter allows the disturbance to pass through. Therefore, there is a deviation in Q_1 and Q_3 in Fig. 12b similar to Fig. 8 in Section 4.3.

Fig. 12c shows that at the largest period of 60 minutes the buffering pressure controller is able to reject the slow flow disturbance without the assistance of the over and under pressure controllers. Therefore, similar to Fig. 12a, there is no deviation in Q_1 or Q_3.

6. Conclusion

This paper investigated the selection of optimal pressure measurement locations with the intent of pressure buffering control in gas headers. The SEM was used to obtain a non-linear model in state-space format which provides the pressure and flow profiles in the header. An EKF was designed to provide estimates of the pressure states along the pipeline. A staggered PI pressure control scheme was applied to control the header pressure and suitable cost functions for flaring, expensive supplier use, and consumer stability were evaluated in a dynamic SOC framework.

It was found that the optimal measurement location is influenced by the disturbance magnitudes and frequencies, the pipe distance from the measurement location to the disturbance source and final control element, and the economic values of the process streams interacting on the header. The results obtained are specific to the selected process layout and control structure but the methodology can be applied to gas headers in general. Furthermore, the insights obtained in this work can be used to aid in the instrumentation design phase of gas headers to aid in pressure transmitter location placement if the control objectives are known.

It was assumed in this work that the design limits are sufficiently far away from the operating conditions. Future work may include design and alarm constraints which will limit the available measurement pairings due to the pipe pressure drop. Additionally, physical pipe design parameters such as the length and operating pressure will also impact the buffering capability. Investigating the extent to which the physical pipe parameters impact the measurement location importance may also prove insightful.

A single header was used for the case study in this paper. Future work may investigate if the methodology presented can be extended to networks of pipelines. i.e. to apply the methodology throughout a general network topology such that the entire network would meet the control and economic goals in an asymptotically stable manner.

The control scheme used in this study is a staggered pressure control approach using PI controllers. However, the control scheme design and tuning will have a large impact on the buffering control performance. Since a detailed process model is available and the disturbance shapes are known, model-based control or feed-forward control schemes may provide better
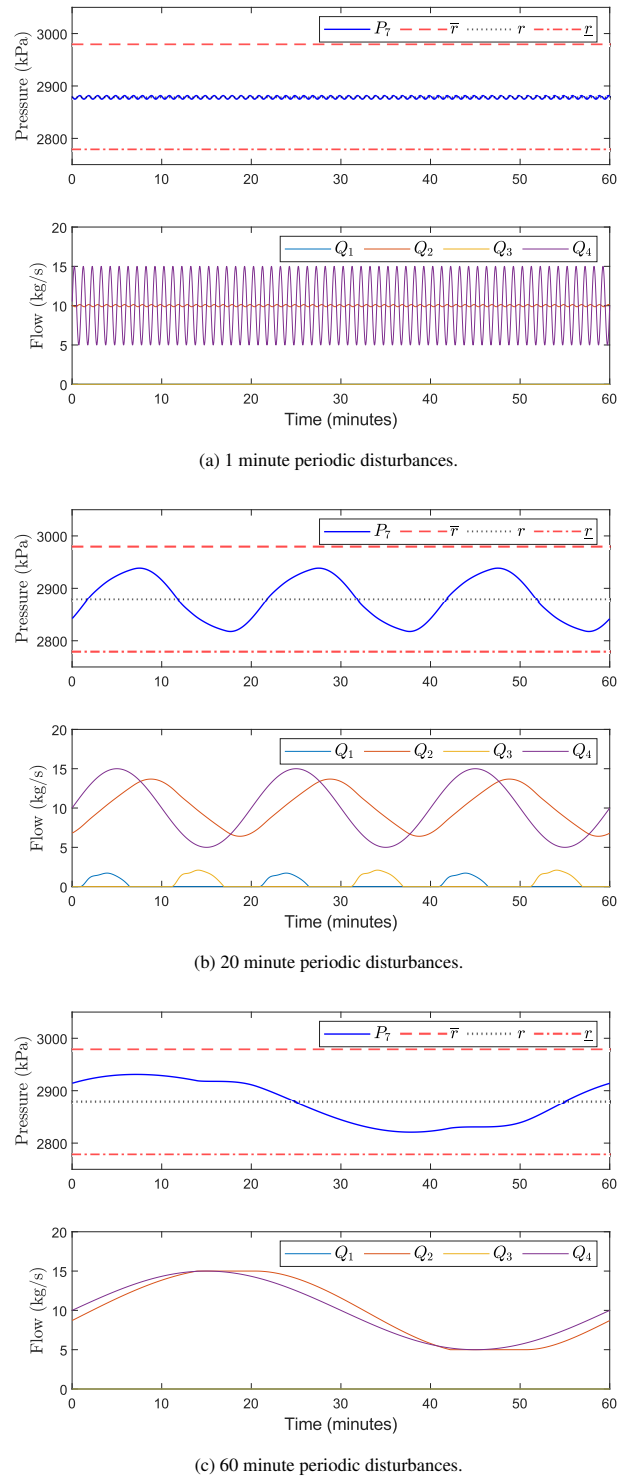

(a) 1 minute periodic disturbances.

(b) 20 minute periodic disturbances.

(c) 60 minute periodic disturbances.

Figure 12: Time domain comparison of sinusoidal disturbances with a magnitude of Q_{max} with periods of 1 minute, 20 and 60 minutes.

performance than PI control. However, the investigation of advanced process control falls outside the scope of this study, future work aims to compare the performance of various advanced process control schemes for gas header buffering control.

References

[1] A. De Klerk, Fischer-Tropsch Refining, John Wiley and Sons, 2012.

[2] J. Lear, G. Barton, J. Perkins, Interaction between process design and process control: the impact of disturbances and uncertainty on estimates of achievable economic performance, Journal of Process Control 5 (1) (1995) 49–62.

[3] L. Ricardez-Sandoval, H. Budman, P. Douglas, Integration of design and control for chemical processes: A review of the literature and some recent results, Annual Reviews in Control 33 (2009) 158–171.

[4] C. L. E. Swartz, Y. Kawajiri, Design for dynamic operation - A review and new perspectives for an increasingly dynamic plant operating environment, Computers & Chemical Engineering 128 (2019) 329–339.

[5] A. Kassidas, J. Patry, T. Marlin, Integrating process and controller models for the design of self-optimizing control, Computers & Chemical Engineering 24 (12) (2000) 2589–2602.

[6] J. Jäschke, Y. Cao, V. Kariwala, Self-optimizing control–a survey, Annual Reviews in Control 43 (2017) 199–223.

[7] S. Skogestad, I. Postlethwaite, Multivariable feedback control analysis and design, 2nd Edition, Wiley, Chichester, England, 2005.

[8] L. Ye, Y. Cao, X. Yuan, Global approximation of self-optimizing controlled variables with average loss minimization, Industrial & Engineering Chemistry Research 54 (48) (2015) 12040–12053.

[9] L. Ye, Y. Cao, S. Skogestad, Global self-optimizing control for uncertain constrained process systems, IFAC-PapersOnLine 50 (1) (2017) 4672–4677.

[10] L. Ye, S. Skogestad, Dynamic self-optimizing control for unconstrained batch processes, Computers & Chemical Engineering 117 (2018) 451–468.

[11] V. de Oliveira, J. Jäschke, S. Skogestad, Null-space method for optimal operation of transient processes, IFAC-PapersOnLine 49 (7) (2016) 418–423.

[12] A. Grema, Y. Cao, Optimal feedback control of oil reservoir waterflooding processes, International Journal of Automation and Computing 13 (1) (2016) 73–80.

[13] K. G. Hanssen, B. Foss, On selection of controlled variables for robust reservoir management, Journal of Petroleum Science and Engineering 147 (2016) 504–514.

[14] A. J. Wiid, J. D. le Roux, I. K. Craig, Modelling of methane-rich gas pipeline networks for simulation and control, Journal of Process Control 92 (2020) 234 – 245.

[15] C. Pozrikidis, Finite and spectral element methods using Matlab, 2nd Edition, Chapman and Hall/CRC, 2014.

[16] J.-F. Mennemann, L. Marko, J. Schmidt, W. Kemmetmüller, A. Kugi, The spectral element method as an efficient tool for transient simulations of hydraulic systems, Applied Mathematical Modelling 54 (2018) 627–647.

[17] M. Chapman, R. Jones, A. J. Pritchard, State observers for monitoring gas pipelines, in: Control of Distributed Parameter Systems, Elsevier, 1983, pp. 333–337.

[18] H. P. Reddy, S. Narasimhan, S. M. Bhallamudi, Simulation and state estimation of transient flow in gas pipeline networks using a transfer function model, Industrial & Engineering Chemistry Research 45 (11) (2006) 3853–3863.

[19] K. Sundar, A. Zlotnik, State and parameter estimation for natural gas pipeline networks using transient state data, IEEE Transactions on Control Systems Technology 27 (5) (2018) 2110–2124.

[20] K. Sundar, A. Zlotnik, Dynamic state and parameter estimation for natural gas networks using real pipeline system data, 2019 IEEE Conference on Control Technology and Applications (CCTA) (2019) 106–111.

[21] A. Benkherouf, A. Allidina, Leak detection and location in gas pipelines, in: IEE Proceedings D-Control Theory and Applications, Vol. 135, IET, 1988, pp. 142–148.

[22] H. Emara-Shabaik, Y. Khulief, I. Hussaini, A non-linear multiple-model state estimation scheme for pipeline leak detection and isolation, Proceedings of the Institution of Mechanical Engineers, Part I: Journal of Systems and Control Engineering 216 (6) (2002) 497–512.

[23] M. Liu, S. Zang, D. Zhou, Fast leak detection and location of gas pipelines based on an adaptive particle filter, International Journal of Applied Mathematics and Computer Science 15 (4) (2005) 541.

[24] H. P. Reddy, S. Narasimhan, S. M. Bhallamudi, S. Bairagi, Leak detection in gas pipeline networks using an efficient state estimator. Part-I: Theory and simulations, Computers & Chemical Engineering 35 (4) (2011) 651–661.

[25] H. P. Reddy, S. Narasimhan, S. M. Bhallamudi, S. Bairagi, Leak detection in gas pipeline networks using an efficient state estimator. Part II. Experimental and field evaluation, Computers & Chemical Engineering 35 (4) (2011) 662–670.

[26] I. Durgut, K. Leblebicioglu, Kalman-filter-based observer design around optimal control policy for gas pipelines, International Journal for Numerical Methods in Fluids 24 (2) (1997) 233–245.

[27] L. Marko, J.-F. Mennemann, L. Jadachowski, W. Kemmetmüller, A. Kugi, Early-and late-lumping observer designs for long hydraulic pipelines: Application to pumped-storage power plants, International Journal of Robust and Nonlinear Control 28 (7) (2018) 2759–2779.

[28] A. Gopalakrishnan, L. T. Biegler, Economic nonlinear model predictive control for periodic optimal operation of gas pipeline networks, Computers & Chemical Engineering 52 (2013) 90–99.

[29] J. P. Berrut, L. N. Trefethen, Barycentric Lagrange interpolation, SIAM Review 46 (2004) 501–517.

[30] A. J. Wiid, J. D. le Roux, I. K. Craig, Non-linear modelling and validation of an industrial methane rich gas network for control applications, 18th European Control Conference, ECC 2019 8795824 (2019) 3126–3131. doi:10.23919/ECC.2019.8795824.

[31] R. Hermann, A. Krener, Nonlinear controllability and observability, IEEE Transactions on Automatic Control 22 (5) (1977) 728–740.

[32] J. D. le Roux, A. Steinboeck, A. Kugi, I. Craig, An EKF observer to estimate semi-autogenous grinding mill hold-ups, Journal of Process Control 51 (2017) 27–41.

[33] K. Wen, Z. Xia, W. Yu, J. Gong, A New Lumped Parameter Model for Natural Gas Pipelines in State Space, Energies 11 (2018) 1971.

[34] P. S. Schermann, Process gains, time lags, reaction curves, in: B. G. Liptak (Ed.), Instrument Engineers' Handbook, Volume 2: Process Control, Third Edition, CRC Press, 1995, Ch. 1.14, pp. 91–101.

[35] S. Skogestad, Simple analytic rules for model reduction and pid controller tuning, Journal of Process Control 13 (4) (2003) 291–309.

[36] A. Reyes-Lúa, C. Backi, S. Skogestad, Improved PI control for a surge tank satisfying level constraints, IFAC-PapersOnLine 51 (2018) 835–840.

[37] M. King, Process Control: A Practical Approach, 2nd Edition, John Wiley and Sons Ltd., West Sussex, United Kingdom, 2016.

Appendix A. Linear Matrices, Poles, and Zeros

The A, B, C, and D matrices linearised at the conditions shown in Table 1 and the corresponding poles and zeros for the system described by (22) are shown below. A brief discussion around the integrating nature of the system is also given.

The A matrix is represented as,

$$A = \left.\frac{\partial \mathbf{f}(\mathbf{x}, \mathbf{u})}{\partial \mathbf{x}^T}\right|_{\mathbf{x}_0, \mathbf{u}_0} = \begin{bmatrix} A_{11} & A_{12} \\ A_{21} & A_{22} \end{bmatrix}.$$

where,

$A_{11} = O_{7x7}$,

$$A_{12} = \begin{bmatrix} -1680 & -2270 & 867 & -281 & 0 & 0 & 0 \\ 454 & 0 & -628 & 173 & 0 & 0 & 0 \\ -173 & 628 & 0 & -454 & 0 & 0 & 0 \\ 140 & -434 & 1140 & -5\text{x}10^{-7} & -1140 & 434 & -140 \\ 0 & 0 & 0 & 454 & 0 & -628 & 173 \\ 0 & 0 & 0 & -173 & 628 & 0 & -454 \\ 0 & 0 & 0 & 281 & -867 & 2270 & 1680 \end{bmatrix},$$

$$A_{21} = \begin{bmatrix} 4.7 & -6.4 & 2.4 & -0.79 & 0 & 0 & 0 \\ 1.3 & 0.012 & -1.8 & 0.49 & 0 & 0 & 0 \\ -0.49 & 1.8 & 0.011 & -1.3 & 0 & 0 & 0 \\ 0.39 & -1.2 & 3.2 & 0.012 & -3.2 & 1.2 & -0.39 \\ 0 & 0 & 0 & 1.3 & 0.013 & -1.8 & 0.49 \\ 0 & 0 & 0 & -0.49 & 1.8 & 0.016 & -1.3 \\ 0 & 0 & 0 & 0.79 & -2.4 & 6.4 & -4.7 \end{bmatrix} \text{x}10^{-4},$$

$$A_{22} = \begin{bmatrix} -0.94 & 0 & 0 & 0 & 0 & 0 & 0 \\ 0 & -0.83 & 0 & 0 & 0 & 0 & 0 \\ 0 & 0 & -0.79 & 0 & 0 & 0 & 0 \\ 0 & 0 & 0 & -0.83 & 0 & 0 & 0 \\ 0 & 0 & 0 & 0 & -0.87 & 0 & 0 \\ 0 & 0 & 0 & 0 & 0 & -0.94 & 0 \\ 0 & 0 & 0 & 0 & 0 & 0 & -0.97 \end{bmatrix}.$$

The matrices B, C, and D are,

$$B = \left.\frac{\partial \mathbf{f}(\mathbf{x}, \mathbf{u})}{\partial \mathbf{u}^T}\right|_{\mathbf{x}_0, \mathbf{u}_0} = \begin{bmatrix} 3400 & 0 \\ 0 & 0 \\ 0 & 0 \\ 0 & 0 \\ 0 & 0 \\ 0 & 0 \\ 0 & -3400 \\ 0.89 & 0 \\ 0 & 0 \\ 0 & 0 \\ 0 & 0 \\ 0 & 0 \\ 0 & 0 \\ 0 & 0.89 \end{bmatrix},$$

$$C = \left.\frac{\partial \mathbf{g}(\mathbf{x}, \mathbf{u})}{\partial \mathbf{x}^T}\right|_{\mathbf{x}_0, \mathbf{u}_0} = \begin{bmatrix} 1 & 0 \\ 0 & 0 \\ 0 & 0 \\ 0 & 0 \\ 0 & 0 \\ 0 & 0 \\ 0 & 1 \\ 0 & 0 \\ 0 & 0 \\ 0 & 0 \\ 0 & 0 \\ 0 & 0 \\ 0 & 0 \\ 0 & 0 \end{bmatrix}^T,$$

$$D = \left.\frac{\partial \mathbf{g}(\mathbf{x}, \mathbf{u})}{\partial \mathbf{u}^T}\right|_{\mathbf{x}_0, \mathbf{u}_0} = O_{2x2} = \begin{bmatrix} 0 & 0 \\ 0 & 0 \end{bmatrix}.$$

The determinant of A is,

$$\det(A) = -9.9562\text{x}10^{-20} \approx 0.$$

A value of 0 indicates that the A matrix is singular which is further confirmed by the rank of A which is less than the amount of states $(2(nN + 1) = 14)$,

$$\text{rank}(A) = 13.$$

The singularity of A shows that at least one of the eigenvalues of A is at the origin. The poles (p_G) and zeros (z_G) of (22) are,

$$p_G = \begin{bmatrix} -0.46 \pm 1.1i \\ -0.47 \pm 1.1i \\ 0^1 \\ -0.071 \\ -0.43 \pm 0.54i \\ -0.43 \pm 0.44i \\ -0.43 \pm 0.14i \\ -0.88 \\ -0.78 \end{bmatrix}, \quad z_G = \begin{bmatrix} -0.33 \pm 0.72i \\ -0.3 \pm 0.59i \\ -0.082 \\ -0.41 \pm 0.45i \\ -0.36 \pm 0.32i \\ -0.89 \\ -0.81 \\ -0.7 \end{bmatrix}.$$

There are no right-half plane (unstable) poles or right-half plane zeros which can impose restrictions on the closed loop performance. The pole at the origin is due to the integrating nature of the header pressures. The size of the matrices and the number of poles and zeros are dependant on the choice of n and N used to spatially discretise the governing equations in (2).

---

[1] value rounded from $1.8\text{x}10^{-16} \approx 0$.